SLAC-PUB-11591
December 2005

ILC EXTRACTION LINE FOR 14 MRAD CROSSING ANGLE*

Y. Nosochkov†, T. Markiewicz, T. Maruyama, A. Seryi, SLAC, Menlo Park, CA 94025, USA
B. Parker, BNL, Upton, NY 11973, USA

Abstract

The earlier studies of the ILC extraction line for 20 mrad and 2 mrad crossing angle options [1]-[5] showed that the 20 mrad design has an advantage of a simpler beamline and lower extraction beam loss because of the independent incoming and extraction optics. However, the large 20 mrad crossing angle requires the use of a crab cavity correction, increases synchrotron radiation emittance growth in the solenoid, and increases photon backscattering from the forward calorimeter of the detector. To reduce these effects, an attempt has been made to minimize the crossing angle while keeping the extraction and incoming lines separate. A new quadrupole scheme near the interaction point has been proposed which allows a reduction of the crossing angle to 14 mrad [6]. The optics design and results of tracking and background simulations for the 14 mrad extraction line are presented.

INTRODUCTION

Preliminary designs of the ILC extraction line for 20 mrad and 2 mrad crossing angles have been developed [1]-[5]. In both designs, the extraction line must transport up to 18.1 MW of the primary disrupted beam and the beamstrahlung (BS) photons to a common or separate dumps without excessive loss on the extraction magnets. These designs also include the dedicated optics for energy and polarization diagnostics.

Comparison of the two designs shows that the 20 mrad option has an advantage of a simpler beamline and lower extraction beam loss because of the independent incoming and extraction optics. However, the disadvantages of the large crossing angle are the stronger dependence of luminosity on a crab cavity correction, the higher synchrotron radiation (SR) emittance growth in the detector solenoid, and the increased photon backscattering from the forward calorimeter of the detector. To reduce these effects, an attempt has been made to minimize the crossing angle while keeping the extraction and incoming lines separate. A new quadrupole scheme near the interaction point (IP) has been proposed which allows a reduction of the crossing angle to 14 mrad [6]. Below, we present the optics design and the results of particle tracking and detector background simulations for the proposed 14 mrad extraction line.

* Work supported by the Department of Energy Contract DE-AC02-76SF00515.

† yuri@slac.stanford.edu

OPTICS

The proposed 14 mrad extraction optics is similar to the 20 mrad design [4] with a few differences described below. In both designs, the extraction optics is separate from the incoming optics, and the primary disrupted e^+/e^- and BS photons travel through the same extraction magnets to one shared dump. In the 20 mrad design, the first incoming and extraction quadrupoles are placed at the same distance, s = 3.51 m after the IP. This is based on the superconducting (SC) compact quadrupole design [7] which makes it possible to have side-by-side quadrupoles in the independent cryostats with a small 70 mm horizontal separation between the beams. However, further reduction of the separation and the crossing angle is not recommended in this option since it would be technically risky and would increase the remnant field outside of the quadrupole on the other beam axis.

To achieve a smaller crossing angle, it was proposed to move the first extraction quadrupole farther from the IP and behind the first incoming quadrupole QD0 [6]. In this case, the separation between the QD0 and the extraction beam pipe can be reduced for the smaller 14 mrad crossing angle. The schematic of the 14 mrad crossing with the nearest to IP incoming and extraction magnets is shown in Fig. 1, where the first extraction quadrupole QDEX1A is placed 6 m after the IP and 0.29 m behind the QD0. As shown in Fig. 2, the QD0 and the extraction pipe are placed in the same cryostat. In this scheme, the QD0 and QDEX1A quadrupoles are actively self-shielded which practically eliminates the remnant field outside of the quadrupole on the other beam axis [6].

One disadvantage of this solution is that the extraction focusing starts later after the IP which tends to increase the beam size in the extraction quadrupoles. However, in this design it was possible to sufficiently increase the gradient of the QDEX1A quadrupole [6] and, therefore, reduce the effect of the missing focusing near the IP.

The lattice functions in the 14 mrad extraction line are shown in Fig.3, where the IP is at $s = 0$ and the dump is at ≈ 400 m. As in the 20 mrad design, the optics consists of the initial DFDF quadrupole system, followed by the two vertical chicanes for energy and polarization diagnostics, and a long drift with three collimators before the dump.

In this optics, the first three extraction quadrupoles are superconducting and are placed between s = 6 m and 11.5 m from IP. They are followed by the dedicated 4 m drift to provide more transverse space for the crab cavity placed on the incoming line at this location. And the warm extraction magnets start at s = 15.5 m. The diagnostic energy and polarization chicanes create local bumps of the

Presented at 36th ICFA Advanced Beam Dynamics Workshop (NANOBEAM 2005) ,
10/17/2005-10/21/2005, Kyoto, Japan

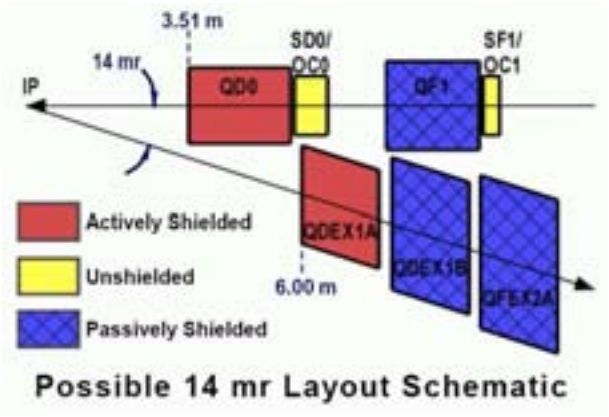

Figure 1: Schematic of the 14 mrad crossing with the incoming and extraction magnets on one side of the IP.

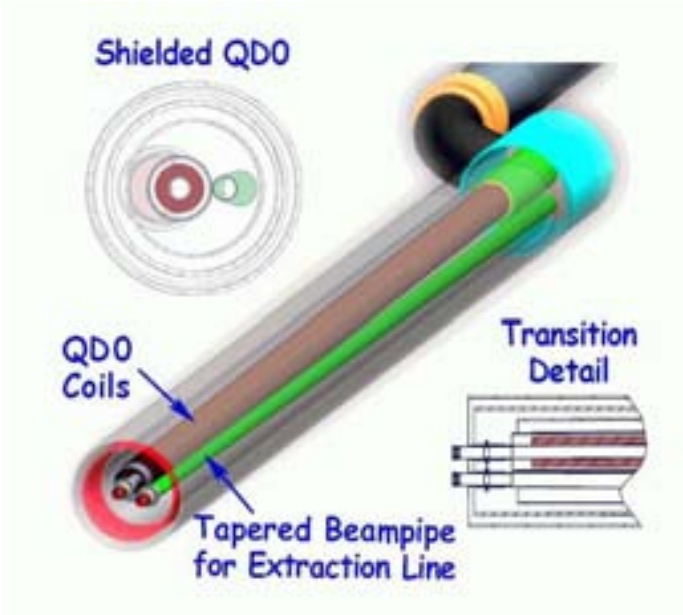

Figure 2: Design drawing of the nearest to IP incoming quadrupole QD0 and the extraction beam pipe in one cryostat.

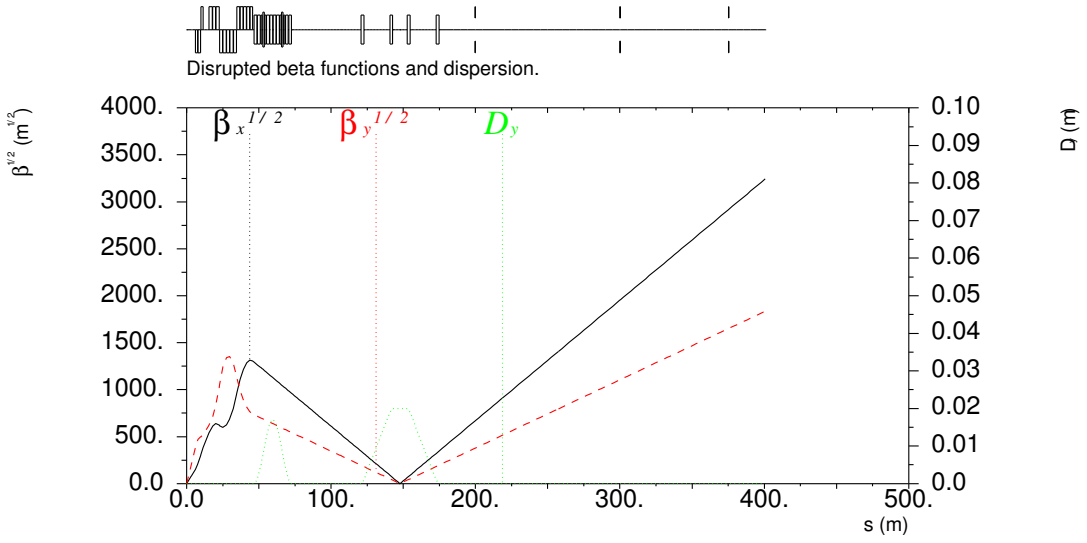

Figure 3: Disrupted beta functions and vertical dispersion in the 14 mrad extraction line. IP is at s = 0.

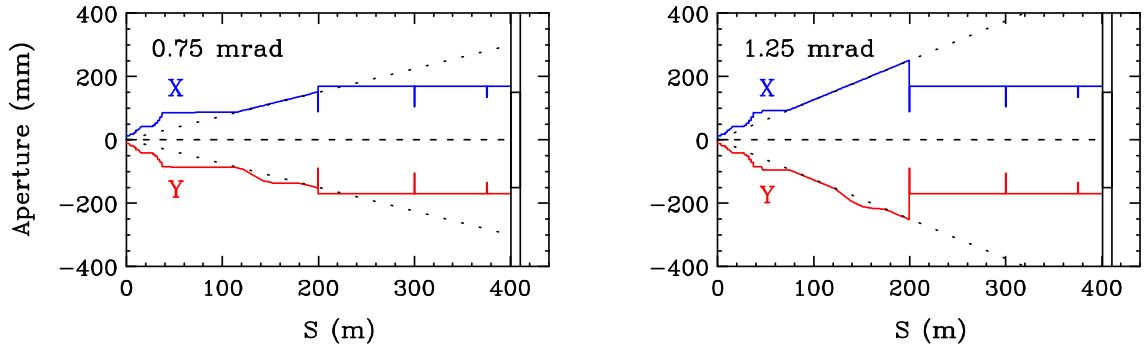

Figure 4: Two models of extraction aperture providing acceptance for the BS photons with the maximum IP angle of ± 0.75 mrad (left) and ± 1.25 mrad (right). The dotted lines show the ± 0.75 mrad and ± 1.25 mrad angles. Three collimators at s $>$ 200 m limit the beam size to 15 cm radius of the dump window.

vertical orbit and vertical dispersion with 1.7 cm and 2 cm peak values, respectively. The optics provides the 2nd focal point at the center of the polarimeter chicane at s $\approx$ 148 m to attain the required $< 100\mu$m RMS beam size for the Compton polarimeter. The horizontal angular transformation term $R_{22} = -0.503$ from IP to the 2nd focus is made close to one of the optimum values (± 0.5) for the polarization measurement. The diagnostic scheme for the 14 mrad extraction is the same as for the 20 mrad design which is described in detail in [3, 8].

In addition to the primary disrupted electron and BS photon beams, the extraction dump must also accept the full power of undisrupted beam if there is no collision at the IP. However, without the disruption, the beam size at the end of the last extraction magnet is too small for the dump window. The final 226 m drift is included to naturally increase the undisrupted beam size in order to avoid damage to the window. However, this long drift also increases the larger sizes of the disrupted electron and BS photon beams. In order to fit the disrupted beam sizes to the specified 15 cm radius of the dump window [9], three round collimators are placed at s $\approx$ 200 m, 300 m and 375 m.

The extraction apertures are made sufficiently large to avoid excessive power loss on the extraction magnets. Because of the large energy spread in the disrupted beam, most of the losses occur in the very low energy tail due to overfocusing in the quadrupoles. For the ILC nominal and high luminosity beam parameter options [10, 11], the size of the quadrupole aperture in the beginning of the extraction line is dominated by the electron beam size. But in the region of chicane bends farther from the IP the photon aperture becomes dominant. Because photons follow the straight lines, the full photon beam size can be rather large far from IP. In the 14 mrad design, we studied two models for the photon aperture in the magnets. In the first model, the magnet apertures were set to accept the photons with the maximum angle of ± 1.25 mrad at IP. This angle corresponds to the maximum photon angle for the ILC nominal and high luminosity options as will be shown below. Therefore, the photons will not be lost on magnets in this case. However, there will be photon losses on the three final collimators which have smaller apertures to limit the beam size at the dump window. In the second model, the magnet apertures were set to accept the photons with a smaller maximum angle of ± 0.75 mrad at IP. The latter has an advantage of smaller and more practical apertures in the magnets far from IP compared to the 1.25 mrad model. Also, the 0.75 mrad photon aperture is favored for the diagnostics [8]. However, both electron and BS photon losses will increase in the bend region in this option. Fig. 4 shows the schematic of these two aperture models. Note that the difference between the models is in the region from s $\approx$ 45 m to 200 m.

Parameters of the 14 mrad extraction quadrupoles are listed in Table 1 for 1 TeV center of mass (CM) energy, where L, B$'$ and R are the length, gradient and aperture radius, respectively. The chicane bends are 2 m long with 0.8339 T field at 1 TeV CM. At 0.5 TeV CM, the magnet field is two times lower.

Table 1: Quadrupole parameters at 1 TeV CM.

Name	L [m]	B$'$ [T/m]	R [mm]
QDEX1A	1.6407	-83.333	18
QDEX1B	1.6407	-50.000	24
QFEX2A	1.6187	+40.000	30
QFEX2B,2C,2D	2.1431	+23.809	42
QDEX3A,3B	2.1058	-23.809	42
QDEX3C	2.1058	-21.739	46
QDEX3D	2.1058	-19.231	52
QDEX3E	2.1058	-16.129	62
QFEX4A	1.9448	+14.084	71
QFEX4B,4C,4D,4E	1.9448	+11.765	85

PARTICLE TRACKING

Simulation of beam transport from the IP to the dump was performed using the DIMAD code [12]. Beam distributions of up to $3.5 \cdot 10^7$ disrupted e^+ and e^- at the IP were generated using the GUINEA–PIG code [13] for the ILC nominal and high luminosity (high-L) options of beam

Table 2: Disrupted beam parameters at the IP for various ILC beam options.

CM energy	Luminosity $[10^{38}]$ $[m^{-2}s^{-1}]$	Beam power [MW]	Δy offset [nm]	Primary electrons E_{min}/E_0 [%]	Primary electrons X'_{max} [μrad]	Primary electrons Y'_{max} [μrad]	BS photons X'_{max} [μrad]	BS photons Y'_{max} [μrad]
0.5 TeV nominal (c11)	2.03	11.3	0	36	529	253	369	212
			200	36	474	674	366	537
0.5 TeV high-L (c15)	4.92	11.3	0	17	1271	431	723	320
			120	17	1280	1415	782	1232
1.0 TeV nominal (c21)	2.81	18.1	0	20	496	159	271	148
			100	19	423	566	279	408
1.0 TeV high-L (c25)	7.81	18.1	0	6.3	2014	489	937	296
			80	6.2	1731	1592	974	1200
1.0 TeV high-L (c26)	5.72	21.7	0	15	661	249	338	170
			100	14	598	696	376	585
1.0 TeV high-L (c27)	4.64	18.1	0	15	597	236	546	159
			100	14	537	691	342	532

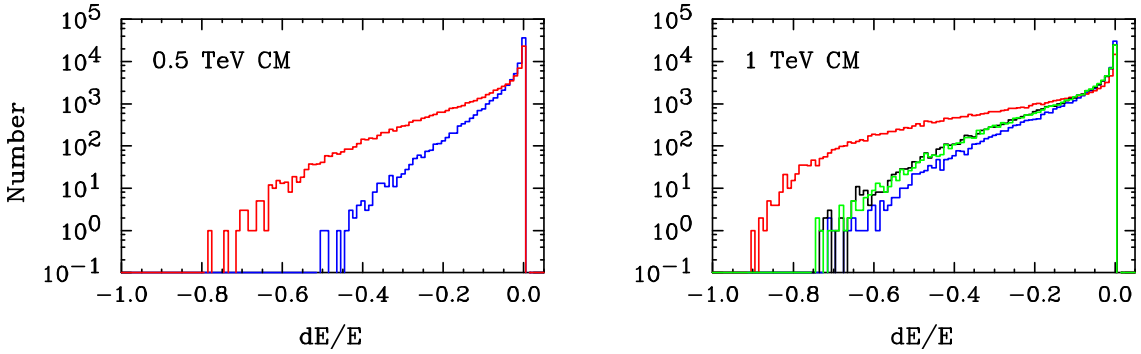

Figure 5: Disrupted energy distribution at IP for the ILC beam options: left figure - c11 (blue), c15 (red); right figure - c21 (blue), c25 (red), c26 (black), c27 (green).

parameters [10] and for the two alternative 1 TeV CM high-L options [11]. Distributions of the BS photons were also generated for each option, but with a lower statistics. In addition, two cases were considered: 1) ideal beam collisions, and 2) collisions with a large vertical beam-to-beam offset Δy which increases the vertical divergence in both the primary and BS photon beams. The value of Δy was selected to maximize this divergence. Summary of the disrupted beam parameters in these options is presented in Table 2. The lowest relative energy E_{min}/E_0 and maximum IP angles in the beam are the critical parameters affecting the loss of primary e^+/e^- and BS photons. Note that the angular and energy spread in the high-L options (c15, c25) are large compared to the other options. The two alternative high-L options (c26, c27) are designed to reduce the energy spread, but at the cost of somewhat lower luminosity. One can see that at the ideal collisions the disrupted beam size is large in the horizontal plane, but the vertical size can dominate at a large Δy offset. The low energy tail increases with the beam energy and luminosity. The disrupted energy distributions for the 0.5 TeV CM and 1 TeV CM options are shown in Fig. 5.

As mentioned earlier, the dump must accept the full power of undisrupted beam. Table 3 shows the x and y RMS sizes of the undisrupted primary beam at the dump at s $\approx$ 400 m. Note that at 0.5 TeV CM the SR effect on the beam size is rather small, but at 1 TeV CM it increases the vertical size more than a factor of 2. At 0.5 TeV CM, the undisrupted beam size satisfies the requirement of $\sigma_x\sigma_y >$ 1.7 mm^2 for a long term survival of the dump window [9]. However, a significantly larger size ($\sim$70 mm^2) is required

Table 3: Undisrupted beam size at dump for various ILC beam options.

CM energy	σ_x [mm]	σ_y [mm]	$\sigma_x\sigma_y$ [mm^2]
0.5 TeV nominal (c11)	3.97	0.43	1.71
0.5 TeV high-L (c15)	5.75	0.52	2.97
1.0 TeV nominal (c21)	2.35	0.78	1.84
1.0 TeV high-L (c25)	4.06	0.79	3.21
1.0 TeV high-L (c26)	2.35	0.75	1.77
1.0 TeV high-L (c27)	2.77	0.75	2.06

Table 4: Disrupted beam power loss in the extraction line for 0.75 mrad photon aperture model.

CM energy	Δy offset [nm]	Total electron loss (kW)				Total BS photon loss (kW)				Electron loss on SC quads [kW]
		Prior to collim.	Collimators			Prior to collim.	Collimators			
			1	2	3		1	2	3	
0.5 TeV nominal (c11)	0	0	0	1.4	0.77	0	0	0.002	0	0
	200	0.0009	3.8	25	2.7	0	0.09	13	0	0
0.5 TeV high-L (c15)	0	2.0	39	230	46	0	1.8	28	0	0.002
	120	15.5	477	584	53	0.48	136	195	0	0
1.0 TeV nominal (c21)	0	0.25	0.46	0.39	0	0	0	0	0	0
	100	2.3	1.1	14	2.1	0	0	0.17	0	0
1.0 TeV high-L (c25)	0	105	32	376	60	0.013	1.2	7.2	0	0.55
	80	256	587	1404	69	0.99	47	276	0	0.58
1.0 TeV high-L (c26)	0	1.8	1.5	1.4	1.4	0	0	0	0	0
	100	10.2	4.2	203	17	0	0.07	2.1	0	0
1.0 TeV high-L (c27)	0	1.3	0.84	0.94	0.15	0	0	0.003	0	0
	100	6.7	4.3	119	8.4	0	0.04	0.90	0	0

Table 5: Disrupted beam power loss in the extraction line for 1.25 mrad photon aperture model.

CM energy	Δy offset [nm]	Total electron loss (kW)				Total BS photon loss (kW)				Electron loss on SC quads [kW]
		Prior to collim.	Collimators			Prior to collim.	Collimators			
			1	2	3		1	2	3	
0.5 TeV nominal (c11)	0	0	0	1.4	0.77	0	0	0.002	0	0
	200	0.0004	3.8	25	2.7	0	0.09	13	0	0
0.5 TeV high-L (c15)	0	1.3	40	230	46	0	1.8	28	0	0.002
	120	5.2	493	585	52	0	137	195	0	0
1.0 TeV nominal (c21)	0	0.11	0.62	0.39	0	0	0	0	0	0
	100	1.4	1.7	14	2.5	0	0	0.17	0	0
1.0 TeV high-L (c25)	0	80	55	377	60	0	1.2	7.2	0	0.55
	80	213	633	1405	67	0	48	276	0	0.58
1.0 TeV high-L (c26)	0	0.93	2.9	1.4	1.4	0	0	0	0	0
	100	6.4	7.2	203	17	0	0.07	2.1	0	0
1.0 TeV high-L (c27)	0	0.66	1.3	0.94	0.15	0	0	0.003	0	0
	100	4.1	6.9	119	8.8	0	0.04	0.90	0	0

to prevent the water boiling in the dump vessel [9]. We consider that a further increase of beam size can be achieved by using a rastering system in front of the dump for sweeping the bunches over a wider area on the dump window. The additional benefit of the rastering system is that the length of the final drift could be significantly reduced, and the dump moved from 400 m after the IP to about 250-300 m. For the same size of the dump window, the closer position of the dump would also naturally open up the apertures of the final collimators and, therefore, reduce the collimator loss. Note that the dump cannot be placed closer than 250 m to IP because of the required minimum separation of 3.5 m between the dump and the incoming beamline.

Summary of the beam loss in the extraction magnets and collimators is presented in Tables 4 and 5 for the 0.75 mrad and 1.25 mrad photon aperture models. The detailed distributions of the primary beam loss in the region of the extraction magnets (prior to collimators) are shown in Fig. 6–16. Note that no losses were observed in the magnet region for the 0.5 TeV CM nominal option (c11) with $\Delta y = 0$. The detector solenoid is not included in the calculation, but the earlier studies [3] showed that it has a small effect on beam loss if the orbit from the solenoid is corrected.

The tracking shows that the most loss in the extraction magnets comes from the lowest energy particles in the primary beam. Typically, the electrons with relative energy of $> 40\%$ will survive in the magnet region regardless of the IP angles. But in the final three collimators with smaller apertures, the losses are due to both the low energy and the large IP angle.

The last column in Tables 4 and 5 shows the primary loss on the SC quadrupoles. It is critical that this loss does not exceed the level of a few Watts. The nominal and the two alternative high-L options did not produce any SC loss

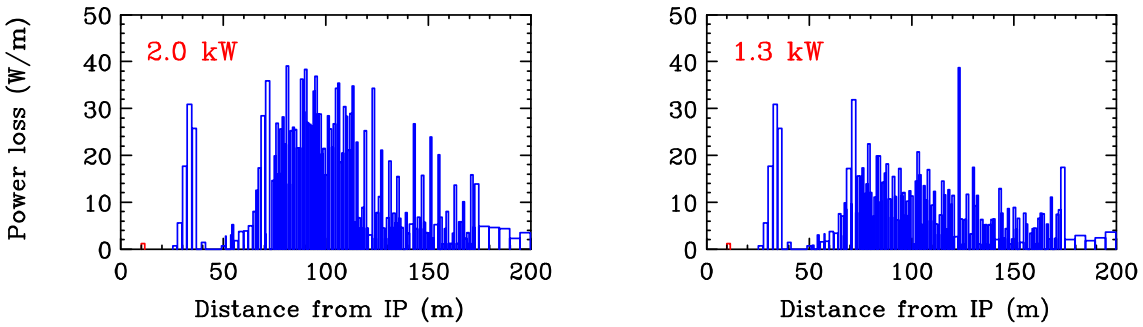

Figure 6: Primary beam loss for 0.5 TeV CM high-L option (c15), $\Delta y = 0$, and 0.75 mrad (left) and 1.25 mrad (right) photon aperture.

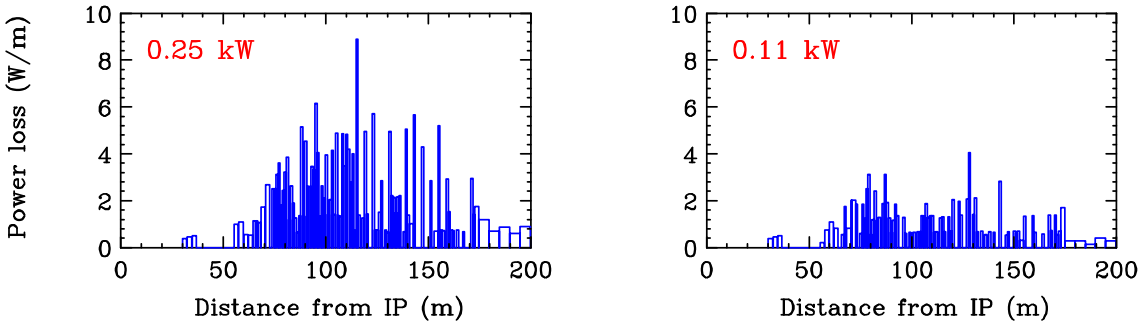

Figure 7: Primary beam loss for 1.0 TeV CM nominal option (c21), $\Delta y = 0$, and 0.75 mrad (left) and 1.25 mrad (right) photon aperture.

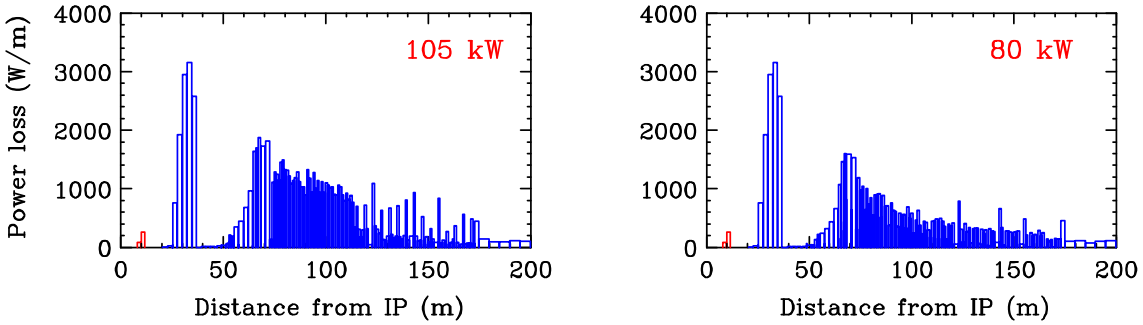

Figure 8: Primary beam loss for 1.0 TeV CM high-L option (c25), $\Delta y = 0$, and 0.75 mrad (left) and 1.25 mrad (right) photon aperture.

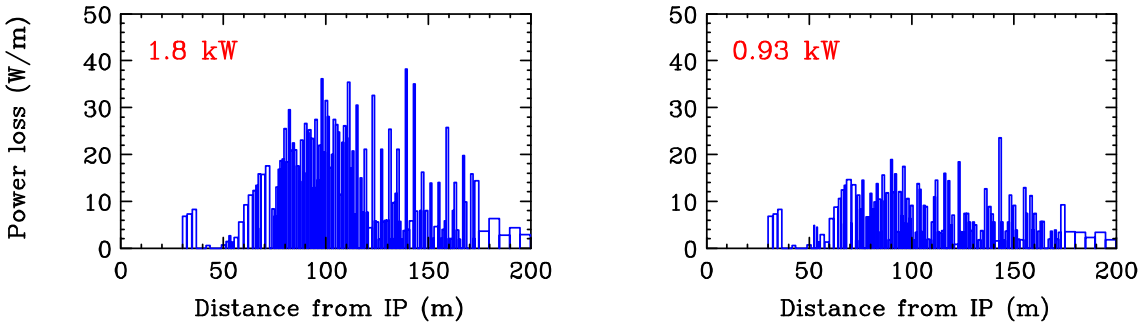

Figure 9: Primary beam loss for 1.0 TeV CM high-L option (c26), $\Delta y = 0$, and 0.75 mrad (left) and 1.25 mrad (right) photon aperture.

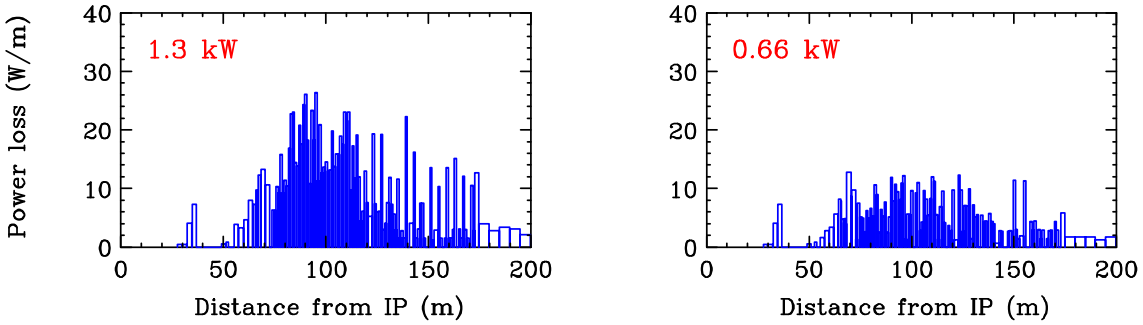

Figure 10: Primary beam loss for 1.0 TeV CM high-L option (c27), $\Delta y = 0$, and 0.75 mrad (left) and 1.25 mrad (right) photon aperture.

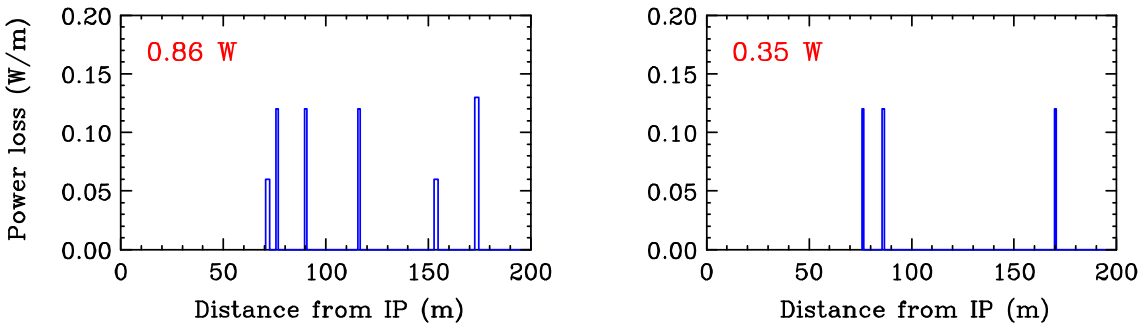

Figure 11: Primary beam loss for 0.5 TeV CM nominal option (c11), $\Delta y = 200$ nm, and 0.75 mrad (left) and 1.25 mrad (right) photon aperture.

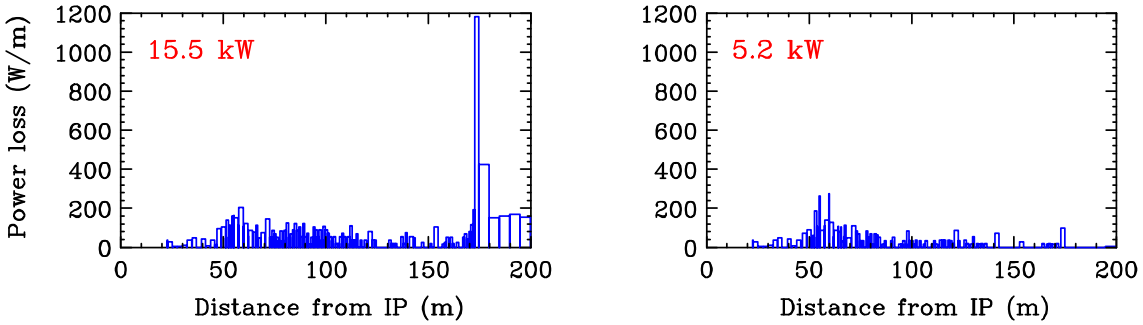

Figure 12: Primary beam loss for 0.5 TeV CM high-L option (c15), $\Delta y = 120$ nm, and 0.75 mrad (left) and 1.25 mrad (right) photon aperture.

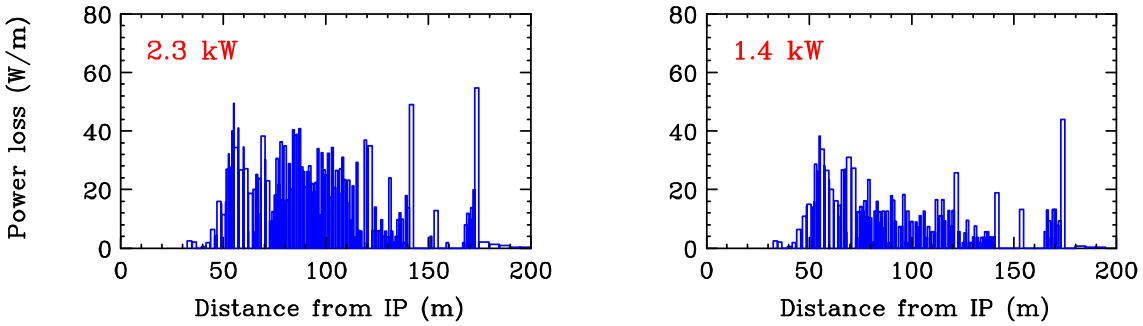

Figure 13: Primary beam loss for 1.0 TeV CM nominal option (c21), $\Delta y = 100$ nm, and 0.75 mrad (left) and 1.25 mrad (right) photon aperture.

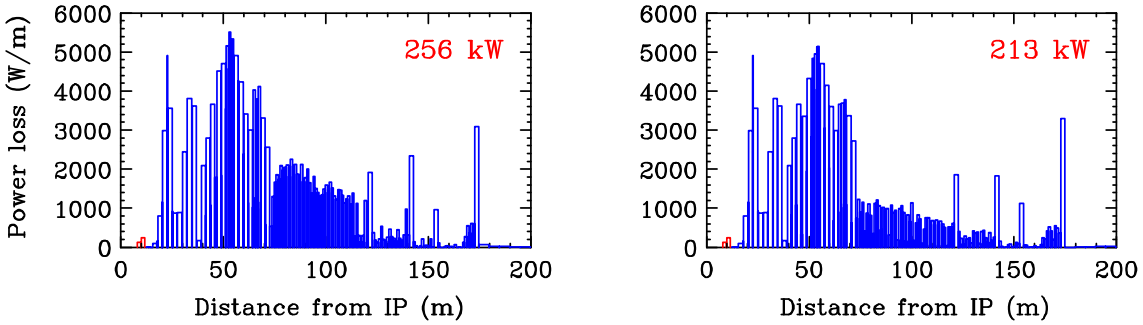

Figure 14: Primary beam loss for 1.0 TeV CM high-L option (c25), $\Delta y = 80$ nm, and 0.75 mrad (left) and 1.25 mrad (right) photon aperture.

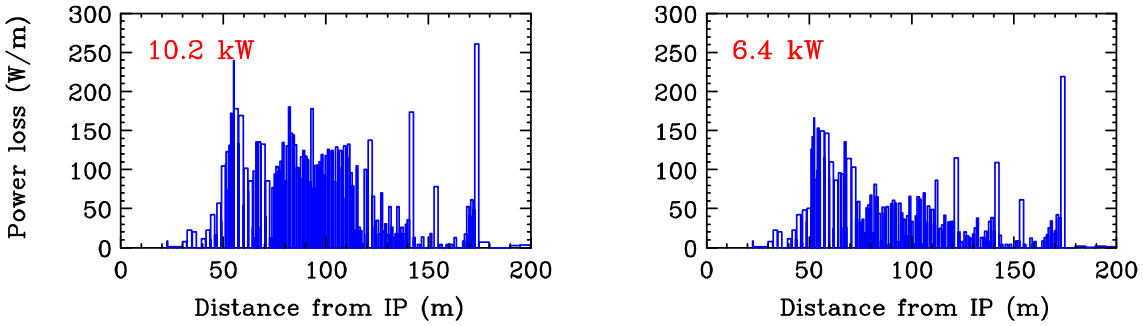

Figure 15: Primary beam loss for 1.0 TeV CM high-L option (c26), $\Delta y = 100$ nm, and 0.75 mrad (left) and 1.25 mrad (right) photon aperture.

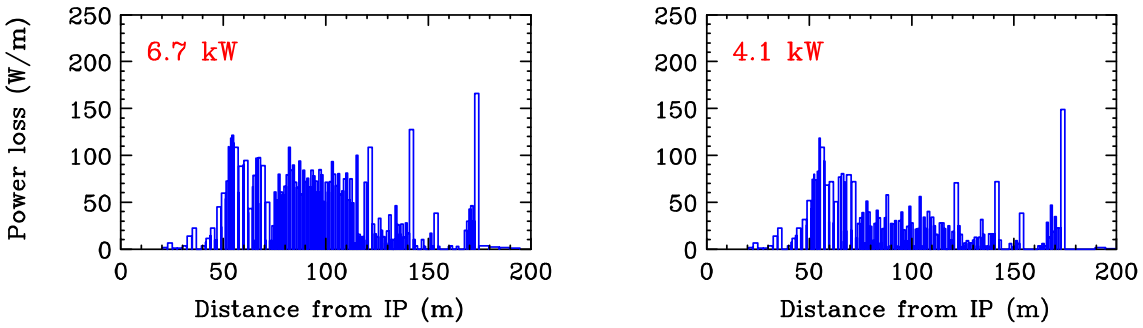

Figure 16: Primary beam loss for 1.0 TeV CM high-L option (c27), $\Delta y = 100$ nm, and 0.75 mrad (left) and 1.25 mrad (right) photon aperture.

in the tracking. In the 1 TeV CM high-L option (c25) the loss on the SC quads is very large and is clearly unacceptable. This option also creates an excessive loss in the downstream warm magnets. This is because of the significant beam power in the low energy tail in this option. In the 0.5 TeV CM high-L option (c15), the primary loss on the SC quads is within 2 W which may be acceptable if the additional losses from secondary particles are minor.

Comparison of the Tables 4 and 5 shows that the primary beam loss on magnets (prior to collimators) is typically a factor of 1.5-2 higher in the 0.75 mrad aperture model due to the smaller aperture in the chicane region. Consequently, the primary loss on the 1st collimator at s $\approx$ 200 m is lower in the 0.75 mrad model since some of the large amplitude particles are lost earlier than in 1.25 mrad model. For both models, the primary loss in the warm magnets is below 1 W in the 0.5 TeV CM nominal option, and below 10 W/m and 60 W/m in the 1 TeV CM nominal option for $\Delta y = 0$ and 100 nm offsets, respectively. In the high-L options, excluding the 1 TeV CM option (c25), the primary loss density is below 40 W/m and 300 W/m for zero and non-zero offsets, respectively. This loss level is considered tolerable for the conventional magnets. One exception is a spike of $\sim$2.4 kW loss in the last polarimeter bend at s $\approx$ 175 m in the 0.5 TeV CM high-L option with $\Delta y = 120$ nm for 0.75 mrad aperture model as shown in Fig. 12. This loss can be reduced by including a protection collimator in front of this bend, however the collimation effects on the diagnostics would have to be checked.

By design, there is no BS photon loss in the extraction quadrupoles for all the nominal and high-L options and for both the 1.25 and 0.75 mrad aperture models. There is also

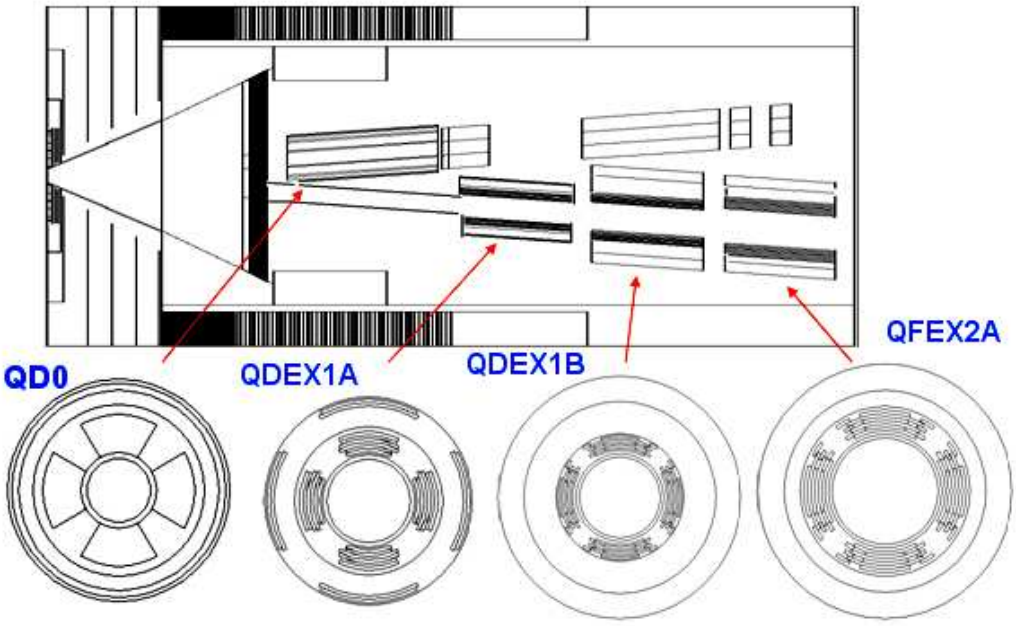

Figure 17: GEANT geometry model used in the background calculation. Top - horizontal view of the nearest to IP incoming and extraction magnets, bottom - cross-sections of the SC quadrupoles.

no BS photon loss in the diagnostic chicanes for the 1.25 mrad aperture model. But there is some photon loss in the chicanes for the 0.75 mrad model in the high-L options (c15 and c25) with large Δy offset, however it is much smaller than the primary electron loss.

The losses of primary electrons and BS photons on the three final collimators are very similar in the 0.75 mrad and 1.25 mrad aperture models. The total collimator loss is moderate in the nominal luminosity options (c11 and c21) and in the alternative 1 TeV CM high-L options (c26 and c27), especially under ideal conditions with $\Delta y = 0$. But the collimator loss is rather high in the 0.5 and 1 TeV high-L options (c15 and c25) due to the large IP divergence for both the disrupted electrons and BS photons. In option (c15) the total collimator loss is 0.35 MW and 1.5 MW for $\Delta y = 0$ and 120 nm, respectively. And in option (c25) it is 0.5 MW and 2.4 MW for $\Delta y = 0$ and 80 nm. Since the collimator loss at $\Delta y = 0$ is dominated by the large horizontal IP angles, one possible way to reduce it is to increase the horizontal size of the dump window and, proportionally, the aperture of the collimators. In this case, the remaining high loss at large Δy should not significantly increase the cumulative loss since the collisions with large offset should be rare. As mentioned earlier, the use of the rastering system could allow to move the dump 100-150 m closer to the IP which would naturally increase the collimator apertures and reduce the collimator loss. In the present setting, the losses are not evenly distributed on the three collimators. With further optimization of the apertures and s-positions of the collimators, and possible enlargement of the dump window size, the maximum loss in the collimators could be further reduced.

Based on these calculations, we conclude that the level of beam loss is acceptable in the nominal options (c11, c21) and 1 TeV CM alternative high-L options (c26, c27). The beam loss is unacceptable in the 1 TeV high-L option (c25), therefore this parameter set should be excluded from consideration. The 0.5 TeV CM high-L option (c15) is tentatively acceptable assuming enlargement of the size of the dump window and the collimator apertures, and with an additional protection collimator at the last bend. The other choice would be to create an alternative 0.5 TeV CM high-L option with reduced IP divergence. Finally, comparison of the two aperture models shows that the increase of beam loss in the extraction magnets due to the reduced aperture in the 0.75 mrad model is acceptable. Because this model also satisfies the diagnostic aperture specifications and significantly reduces the bend apertures, we consider it the preferred model.

DETECTOR BACKGROUND

The incoming and extraction magnets within approximately 20 m of IP were modeled in the GEANT 3 code, and the detector background from the incoherently produced e^+e^- pairs was calculated for the SiD detector. Figure 17 shows the GEANT geometry model used in the calculation. The materials and geometries of the self-shielded magnets are represented in the model. The detector and masking scheme are described in [14]. The VXD layers are at the radial and longitudinal positions of r = 1.4, 2.6, 3.7, 4.8, 6.0 cm and |z| = 6.25 cm. The e^+e^- pairs were generated using the GUINEA–PIG code [13] for the ILC 0.5 TeV nominal beam parameters.

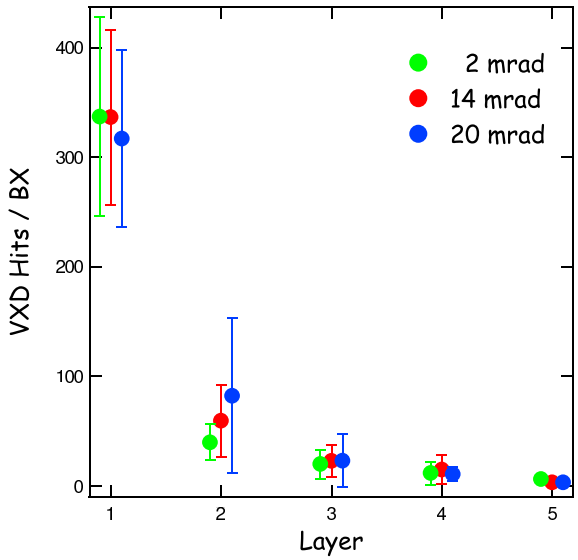

Figure 18: Calculated number of charge particle hits per bunch crossing in the vertex detector layers for the 2 mrad, 14 mrad, and 20 mrad crossing angle schemes.

Figure 18 compares the calculated number of charge particle hits per bunch crossing in the vertex detector layers for the 2 mrad [5], 14 mrad, and 20 mrad [4] crossing angle schemes. The average and RMS values are calculated from 20 statistically independent bunches. Since the majority of VXD hits are due to the low energy e^+/e^- directly hitting the VXD layers, and the contribution from the secondary e^+/e^- backscattered from the very forward calorimeter (BeamCal) is small, the number of VXD hits is not very dependent on the crossing angle. There is, however, about 30% of bunch-to-bunch fluctuation, but the crossing angle dependence is certainly smaller than this fluctuation. For 20 mrad crossing, a detector-integrated-dipole (DID) field is proposed for compensation of the detector solenoid field on the incoming beam orbit [15]. The DID field, however, increases the effect on the extraction beam. One advantage of the smaller 14 mrad angle is that the effects of synchrotron radiation, detector solenoid and DID field are reduced compared to 20 mrad crossing. On the other hand, one can reverse the DID field to correct the extraction beam rather than the incoming beam (anti-DID). In this case, the field strength of the anti-DID is optimized in order to maximize the number of pairs into the extraction hole. The number of charge particle hits in the VXD detector was calculated using the DID and anti-DID options, but the DID field dependence was found negligible.

When e^+e^- pairs hit BeamCal, secondary photons are generated, which will form a secondary background in the VXD and silicon trackers. The secondary photon production is proportional to the amount of energy deposited in BeamCal. This energy is highly dependent on the crossing angle and the radius of the beam holes in BeamCal. Furthermore, this energy is also dependent on the DID field for the 14 mrad and 20 mrad crossing angles. Figure 19

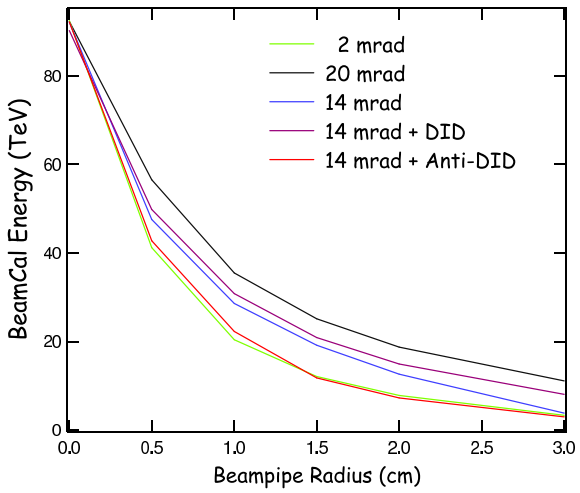

Figure 19: Total energy in BeamCal as a function of the extraction beam hole radius.

shows the total energy in BeamCal as a function of the extraction beam hole radius. There is only one beam hole for the 2 mrad crossing scheme, while the radius of the incoming beam hole is fixed to 1 cm for the 14 mrad and 20 mrad crossing schemes. Without the DID field, the energy for 14 mrad angle is about 25% smaller than that for 20 mrad at r = 1.5 cm used in the detector background calculations. With the anti-DID field, the energy for 14 mrad angle is reduced and becomes comparable to that for 2 mrad. The number of secondary photons in the silicon tracker is 1800 per bunch crossing for the 14 mrad crossing, and this number decreases to 800 with the anti-DID, which is comparable to 700 for the 2 mrad scheme.

CONCLUSION

The presented design of the ILC 14 mrad extraction line is based on the 20 mrad design and the new quadrupole scheme near the IP. Compared to the 2 mrad design, the 14 mrad option maintains the advantages of the separate extraction beamline, a simpler optics and lower beam loss as in the 20 mrad design. However, it also reduces the negative effects of the large crossing angle. With the smaller 14 mrad angle, the luminosity dependence on the crab cavity correction is reduced. Additionally, the SR emittance growth in the solenoid and the photon backscattering from the forward calorimeter of the detector are reduced. With the use of the anti-DID correcting field these detector backgrounds can be as small as in the 2 mrad design. The tracking simulations showed that the losses of primary electrons and BS photons are acceptable in the considered nominal and high-L options except the 1 TeV CM high-L option (c25) which should be excluded from consideration. Further optimization and enlargement of aperture of the final collimators and the dump window are considered for the reduction of beam loss on the collimators in the 0.5 TeV CM high-L option (c15).

REFERENCES

[1] Y. Nosochkov, *et al.*, SLAC–PUB–11363 (2005), presented at the LCWS 2005, Stanford, CA, USA (2005).

[2] R. Appleby, *et al.*, SLAC–PUB–11372 (2005), presented at the LCWS 2005, Stanford, CA, USA (2005).

[3] Y. Nosochkov, *et al.*, SLAC–PUB–11205 (2005), presented at the PAC 2005, Knoxville, TN, USA (2005).

[4] Y. Nosochkov, *et al.*, presented at the Snowmass ILC Workshop 2005, Snowmass, CO, USA (2005), http://alcpg2005.colorado.edu:8080/alcpg2005/program/accelerator/WG4/aug17_nosochkov_extraction20mrad.pdf .

[5] Y. Nosochkov for the SLAC-BNL-UK-France Task Force, presented at the Snowmass ILC Workshop 2005, Snowmass, CO, USA (2005), http://alcpg2005.colorado.edu:8080/alcpg2005/program/accelerator/WG4/aug17_nosochkov_extraction2mrad.pdf .

[6] B. Parker, "Recent Progress Designing Compact Superconducting Final Focus Magnets for the ILC," these proceedings.

[7] B. Parker, *et al.*, "Compact Superconducting Final Focus Magnet Options for the ILC," presented at the PAC 2005, Knoxville, TN, USA (2005).

[8] K.C. Moffeit, *et al.*, SLAC–PUB–11322 (2005), presented at the LCWS 2005, Stanford, CA, USA (2005).

[9] D. Walz, presented at the Snowmass ILC Workshop 2005, Snowmass, CO, USA (2005), http://alcpg2005.colorado.edu:8080/alcpg2005/program/accelerator/WG4/aug17_beam_dump_d_walz.pdf .

[10] T. Raubenheimer, http://www-project.slac.stanford.edu/ilc/acceldev/beamparameters.html (February 28, 2005).

[11] A. Seryi, presented at the Snowmass ILC Workshop 2005, Snowmass, CO, USA (2005), http://alcpg2005.colorado.edu:8080/alcpg2005/program/accelerator/GG1/aug17_seryi_high_lumi_pars.ppt .

[12] http://www.slac.stanford.edu/accel/ilc/codes/dimad/ .

[13] D. Schulte, "Beam-Beam Simulations with GUINEA–PIG," ICAP98, Monterey, CA, USA (1998).

[14] T.W. Markiewicz and T. Maruyama, SLAC-PUB-10465, presented at the 5th International Workshop on Electron-Electron Interactions at TeV Energies, Santa Cruz, CA, USA (2004).

[15] B. Parker and A. Seryi, SLAC–PUB–11038 (2005).